Computers & Structures Vol. 38, No. 5/6, pp. 637–651, 1991
Printed in Great Britain.

0045-7949/91 $3.00 + 0.00
© 1991 Pergamon Press plc

NONLINEAR FINITE ELEMENT ANALYSIS OF REINFORCED CONCRETE PLATES AND SHELLS UNDER MONOTONIC LOADING

H.-T. Hu† and W. C. Schnobrich‡

†National Center for Composite Materials Research, University of Illinois, Urbana, IL 61801, U.S.A.

‡Department of Civil Engineering, University of Illinois, Urbana, IL 61801, U.S.A.

(*Received* 20 *February* 1990)

Abstract—Plane stress constitutive models are proposed for the nonlinear finite element analysis of reinforced concrete structures under monotonic loading. An elastic strain hardening plastic stress–strain relationship with a nonassociated flow rule is used to model concrete in the compression dominating region and an elastic brittle fracture behavior is assumed for concrete in the tension dominating area. After cracking takes place, the smeared cracked approach together with the rotating crack concept is employed. The steel is modeled by an idealized bilinear curve identical in tension and compressions. Via a layered approach, these material models are further extended to model the flexural behavior of reinforced concrete plates and shells. These material models have been tested against experimental data and good agreement has been obtained.

NOTATION

$[C]_c$	rotating crack tangent constitutive matrix for concrete
$[C]_e, [C]_p, [C]_{ep}$	elastic, plastic and elastic–plastic material matrices
$[C]_{si}$	constitutive matrix of the ith steel layer in material coordinates
$[C']$	constitutive matrix of cracked concrete in crack coordinates
$[C]$	constitutive matrix for transverse shear
$[C]_i, [C]_j$	inplane constitutive matrixes for individual steel layer and individual concrete layer
$[D]$	8 by 8 constitutive matrix for stress resultants
E_c, E_t	initial modulus and tangent modulus for concrete
E_s, E_{sp}	elastic modulus and plastic modulus of steel
$F(\ ), G(\ )$	loading functions
$[G]$	matrix that reflects the possible changes in the crack direction
G, G_c	shear moduli of uncracked and cracked concrete
$\{N\}, \{M\}, \{Q\}$	vectors of stress resultants
$[T(\ )]$	transformation matrix
$f(\ ), g(\ )$	yield function and plastic potential function
f_c, f_t	compressive stress and tensile stress of concrete
f'_c, f'_t	maximum compressive strength and maximum tensile strength of concrete
f_{cm}	degraded maximum compressive stress of concrete
f_{si}, f_{yi}	current stress and yield stress for ith steel layer
(x, y)	global coordinates
(x', y')	material coordinates or crack coordinates
z_{jt}, z_j, z_{jb}	distance from the middle surface to the top, middle and bottom of the jth layer
α'	correction factor for shear
$\{\epsilon\} = \{\epsilon_x, \epsilon_y, \epsilon_{xy}\}$	strain vector in global coordinates
$\{\epsilon_o\} = \{\epsilon_{xo}, \epsilon_{yo}, \epsilon_{xyo}\}$	vector of middle surface strain
ϵ_f, σ_f	maximum strain and corresponding stress on the uniaxial stress–strain curve
ϵ_o	strain corresponding to f'_c in a uniaxial compression test
ϵ_t	tensile strain of concrete
ϵ_*	strain corresponding to f'_c on the equivalent uniaxial stress–strain curve
ϕ	angle measured counterclockwise in degrees from strong reinforcement direction to crack direction
ϕ_i	angle between the ith steel axis and the global x-axis
$\{\gamma_t\} = \{\gamma_{xz}, \gamma_{xz}\}$	vector of transverse shear strain
$\{\kappa\} = \{\kappa_x, \kappa_y, \kappa_{xy}\}$	vector of curvature
θ	rotational angle between the global coordinates and the crack coordinates
θ_i	angle between the ith steel axis and the direction normal to crack
μ	shear retention factor
ν	Poisson's ratio of concrete
ρ_i	steel percentage for ith steel layer
$\{\sigma\} = \{\sigma_x, \sigma_y, \sigma_{xy}\}$	stress vector in global coordinates
$\bar{\sigma}, \bar{\epsilon}$	equivalent stress and equivalent strain
σ_m, τ_{oct}	mean stress and octahedral shear stress
σ'_x, σ'_y	stresses of concrete in crack coordinates
σ_1, σ_2	maximum and minimum principal stresses
$\{\ \}, \{\ \}^T, [\ ]$	row vector, column vector and matrix

1. INTRODUCTION

Structural design of reinforced concrete plates and shells is usually based either on forces determined using a linear elastic analysis or by selecting a mechanism using yield line theory. Concrete plasticity, cracking, tension stiffening, and other nonlinear material behaviors are commonly ignored during the elastic analysis or grossly approximated in the yield line approach. Today, with the help of the computer, it is possible to carry out a finite element analysis, rationally simulating such nonlinear behavior. However, the success of such an analysis depends on a thorough understanding and modeling of the composite material behavior.

For plates and shells, the stress state at any location can be approximated as being in a state of plane stress. In previous papers by the present authors [1, 2], the constitutive equations of reinforcing steel, plain concrete and cracked reinforced concrete under such plane stress conditions have been developed and tested against the data reported from several experimental studies. The consequence of these comparisons shows good correlation between the experimental and comparable computed quantities. In this paper, those constitutive models are briefly summarized (detailed discussion of those models can be obtained in [1] and [2]). Then, through a layered approach, they are further extended to model flexural behavior or combined membrane–flexural behavior of reinforced concrete plate and shell structures.

In the layered approach, the concrete section is divided up through the thickness into a number of layers. Each layer is assumed to be in a state of plane stress. The proposed material models are then applied to each layer individually. In order to demonstrate the capability and generality of the proposed material models in flexural as well as combined membrane– flexural applications, a series of numerical examples is presented and compared with experimental results.

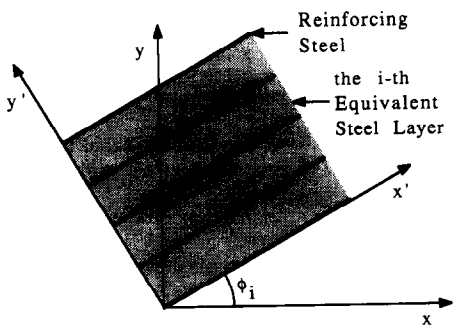

Fig. 1. Equivalent steel layer and material coordinates for steel.

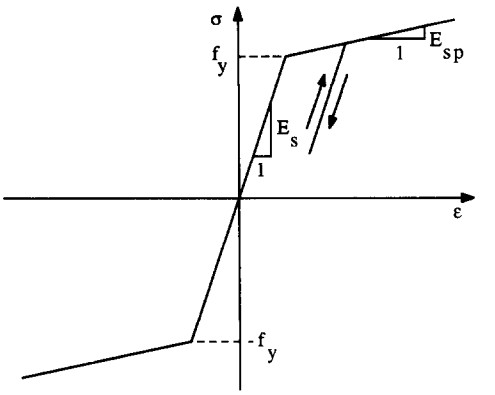

Fig. 2. Idealized stress–strain curve for steel.

2. CONSTITUTIVE MATRIX FOR REINFORCING STEEL

Reinforcing steel is treated as an equivalent uniaxial layered material placed at the depth of the centerline of the bars and smeared out horizontally over the region of bar effect (Fig. 1). As many layers are used as there are layers of bars in the cross section, each with its uniaxial properties oriented along the axis of the bars. The stress–strain curve of reinforcing steel is modeled by an idealized bilinear curve identical in tension and compression (Fig. 2). The dowel action of the reinforcing steel is neglected and the bond between steel and concrete is assumed to remain perfect. The incremental constitutive matrix for the ith steel layer, $[C]_{si}$, in the material coordinates (x', y'), as shown in Fig. 1, can be written as

$$[C]_{si} = \begin{bmatrix} \rho_i E_s & 0 & 0 \\ 0 & 0 & 0 \\ 0 & 0 & 0 \end{bmatrix}, \tag{1}$$

where ρ_i and E_s are the steel percentage and the modulus of elasticity of the reinforcement in the ith layer. When yielding of steel occurs, the incremental constitutive matrix reverts to

$$[C]_{si} = \begin{bmatrix} \rho_i E_{sp} & 0 & 0 \\ 0 & 0 & 0 \\ 0 & 0 & 0 \end{bmatrix}, \tag{2}$$

where E_{sp} is the plastic modulus for steel.

3. YIELD FUNCTIONS AND HARDENING RULE

The use of a plasticity model to describe the behavior of concrete is recognized as an approximation of convenience. It is realized that concrete is

not a real elastic–plastic material but introducing softening through plasticity provides a mathematically defined description of that softening that is in reasonable agreement with experimental data. For plate and shell type structures in particular, the more critical items are the amount and placement of the steel. Precision in the definition of the softening on the compression side is not critical in most cases. The fact that there is softening must be acknowledged but what precise rules govern that softening is not critical. A simple mathematically well defined set is most logical and that translates to a plasticity theory.

In this investigation, the theory of plasticity is employed to describe the strain hardening behavior of plain concrete. The initial and subsequent yield surface assumed for the concrete (Fig. 3) can be defined by the same yield function expressed in the following form [1]:

$$f(\{\sigma\}, \sigma) = F(\{\sigma\}) - \sigma = 0, \tag{3}$$

where $\{\sigma\} = \{\sigma_x, \sigma_y, \tau_{xy}\}$ is a stress vector. The function F can be looked upon as a loading function and σ is a hardening parameter called the 'equivalent stress'.

For biaxial tension, the type of concrete failure is cracking. It is assumed that the initial yield surface coincides with the failure surface (Fig. 3). Under this assumption, concrete behaves in a purely linear elastic fashion up to failure with no plastic deformation having occurred. The failure surface for biaxial tension is defined as

$$f = c\left(\frac{3}{2\sqrt{2}}\frac{1+\alpha}{\alpha}\tau_{oct} + \frac{3}{2}\frac{1-\alpha}{\alpha}\sigma_m\right) - f'_c = 0, \tag{4}$$

where f'_c is the maximum compressive strength of concrete. σ_m and τ_{oct} are the mean and octahedral shear stresses, respectively. For plane stress conditions, these have the following forms:

$$\sigma_m = \tfrac{1}{3}(\sigma_x + \sigma_y)$$

$$\tau_{oct} = \frac{\sqrt{2}}{3}(\sigma_x^2 - \sigma_x\sigma_y + \sigma_y^2 + 3\tau_{xy}^2)^{1/2}.$$

In eqn (4), $\alpha = f'_t/f'_c \approx 0.09$, where f'_t is the maximum tensile strength of concrete. The variable c is determined by the following equation:

$$c = 1 - 0.4019(\sigma_2/\sigma_1) + 0.008913(\sigma_2/\sigma_1)^2,$$

where σ_1 and σ_2 are principal stresses with $\sigma_1 \geqslant \sigma_2$.

When concrete is subjected to a combined tension–compression stress state, the yield function is defined as

$$f = c\left(\frac{3}{2\sqrt{2}}\frac{1+\alpha}{\alpha}\tau_{oct} + \frac{3}{2}\frac{1-\alpha}{\alpha}\sigma_m\right) - \sigma = 0, \tag{5}$$

where for $-\infty < \sigma_1/\sigma_2 < -0.103$

$$c = 1 - 0.02886(\sigma_2/\sigma_1) - 0.006657(\sigma_2/\sigma_1)^2 - 0.0002443(\sigma_2/\sigma_1)^3,$$

while for $-0.103 \leqslant \sigma_1/\sigma_2 < 0$

$$c = 1 + 6.339(\sigma_1/\sigma_2) + 68.82(\sigma_1/\sigma_2)^2 + 183.8(\sigma_1/\sigma_2)^3.$$

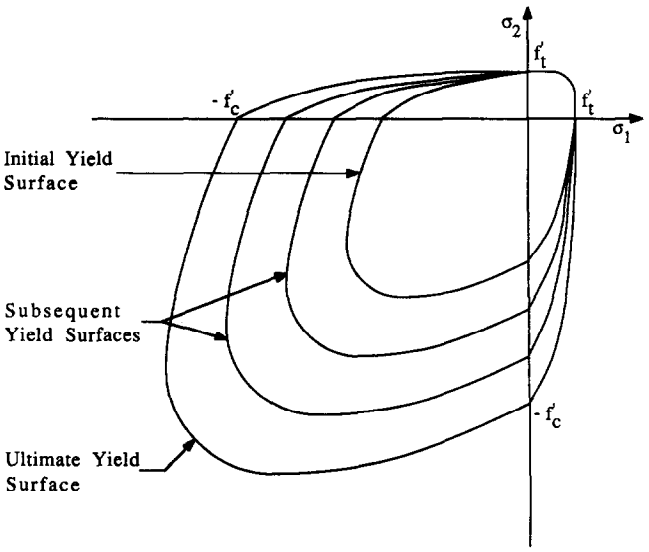

Fig. 3. Yield surface of concrete in the two dimensional principal stress plane.

is relatively large while crushing failure takes place under high compression–low tension stress states. In order to separate these two failure modes, the principal stress ratio σ_1/σ_2 of $1/-15$ reported by Kupfer *et al.* [3] is used. Thus, when $-\infty < \sigma_1/\sigma_2 < -1/15$ and $\sigma = f'_c$, cracking will occur; and when $-1/15 \leqslant \sigma_1/\sigma_2 < 0$ and $\sigma = f'_c$, concrete will enter the descending portion of its stress–strain curve which then leads to the crushing condition.

For biaxial compression, the type of concrete failure is crushing and the yield function is defined as

$$f = c\left(\frac{3}{\sqrt{2}}\frac{2\beta-1}{\beta}\tau_{oct} + 3\frac{\beta-1}{\beta}\sigma_m\right) - \sigma = 0, \quad (6)$$

where $\beta = 1.16$ and

$$c = 1 + 0.05848(\sigma_2/\sigma_1) - 0.05848(\sigma_2/\sigma_1)^2.$$

The hardening rule defines the motion of the subsequent yield surfaces during plastic loading. In this study, an isotropic hardening is used. This assumed that the yield surface expands uniformly without distortion as plastic deformation occurs, as shown schematically in Fig. 4. It is known that the Bauschinger effect cannot be modeled with an isotropic hardening rule. However, under monotonic loading conditions, the Bauschinger effect is not crucial because no reverse loading takes place. As a consequence, an isotropic hardening rule is adequate in modeling the hardening behavior of concrete under monotonic loading conditions.

4. EQUIVALENT UNIAXIAL STRESS–STRAIN CURVE

When plastic deformation does occur, there should be a certain parameter to guide the expansion of the yield surface. A commonly used approach is to relate the multidimensional stress and strain conditions to a pair of quantities, namely, the equivalent stress σ and equivalent strain ϵ, such that results obtained following different loading paths can all be correlated by means of an equivalent uniaxial stress–strain curve.

The equivalent uniaxial stress–strain curve used in this study has the following form [1, 4]:

$$\sigma = \frac{E_c\epsilon}{1 + (R + R_E - 2)\left(\frac{\epsilon}{\epsilon_*}\right) - (2R-1)\left(\frac{\epsilon}{\epsilon_*}\right)^2 + R\left(\frac{\epsilon}{\epsilon_*}\right)^3}, \quad (7)$$

in which

$$R = \frac{R_E(R_\sigma - 1)}{(R_\epsilon - 1)^2} - \frac{1}{R_\epsilon} \qquad R_E = \frac{E_c}{E_o} \qquad R_\sigma = f'_c/\sigma_f \qquad R_\epsilon = \epsilon_f/\epsilon_* \qquad E_o = f'_c/\epsilon_*.$$

In eqn (7) $\epsilon_* = q\epsilon_o$ is the strain corresponding to f'_c on the equivalent uniaxial stress–strain curve (Fig. 5), while ϵ_o is the strain corresponding to f'_c as observed in a uniaxial compression test. E_c is the initial modulus of elasticity. ϵ_f and σ_f are the maximum strain and the corresponding stress on the equivalent uniaxial stress–strain curve.

The value of the variable q can be determined as follows (with $\sigma_1 \geqslant \sigma_2$).

(1) In a combined tension–compression region, for $-\infty < \sigma_1/\sigma_2 < -0.103$

$$q = \frac{f'_c}{E_c\epsilon_o} + \left(1 - \frac{f'_c}{E_c\epsilon_o}\right)[0.001231(\sigma_2/\sigma_1) + 0.001469(\sigma_2/\sigma_1)^2 + 0.00001340(\sigma_2/\sigma_1)^3]$$

for $-0.103 \leqslant \sigma_1/\sigma_2 < 0$

$$q = \frac{f'_c}{E_c\epsilon_o} + \left(1 - \frac{f'_c}{E_c\epsilon_o}\right)[1 + 13.96(\sigma_1/\sigma_2) + 59.21(\sigma_1/\sigma_2)^2 + 69.24(\sigma_1/\sigma_2)^3].$$

(2) In a biaxial compression region

$$q = \frac{f'_c}{E_c\epsilon_o} + \left(1 - \frac{f'_c}{E_c\epsilon_o}\right)[1 + 1.782(\sigma_1/\sigma_2) + 0.5936(\sigma_1/\sigma_2)^2].$$

For the values of σ_f and ϵ_f, Darwin and Pecknold [5] used $R_\sigma = 5$, $R_\epsilon = 4$; Elwi and Murray [6] and Chen [7] used $R_\sigma = 4$, $R_\epsilon = 4$. Generally, to define σ_f and ϵ_f on any rigorous experimental basis is impossible, because

the descending branch of the stress–strain curve is highly test dependent and is usually unavailable from statically determinate tests. In this study, it is assumed that $R_\sigma = 4$ and $R_\epsilon = 4$.

The equivalent uniaxial tangent modulus E_t can be calculated by differentiating eqn (7) with respect to the equivalent strain ϵ. The result has the following form:

$$E_t = \frac{d\sigma}{d\epsilon} = \frac{E_c\left[1 + (2R-1)\left(\frac{\epsilon}{\epsilon_*}\right)^2 - 2R\left(\frac{\epsilon}{\epsilon_*}\right)^3\right]}{\left[1 + (R + R_E - 2)\left(\frac{\epsilon}{\epsilon_*}\right) - (2R-1)\left(\frac{\epsilon}{\epsilon_*}\right)^2 + R\left(\frac{\epsilon}{\epsilon_*}\right)^3\right]^2}. \quad (8)$$

Beyond the peak stress point in the strain softening region, with further straining, the compressive stress begins to decrease and the equivalent uniaxial tangent modulus becomes negative. In order to prevent the numerical difficulties associated with a negative tangent modulus, once the ultimate stress f'_c has been reached, E_t is set to zero and concrete then behaves like a perfectly plastic material. The accumulated unbalanced stresses are released in a stepwise fashion with the corresponding yield surface being contracted simultaneously.

5. CONSTITUTIVE EQUATIONS FOR PLASTIC CONCRETE

Once the yield functions have been defined, the hardening rule has been selected, and the equivalent uniaxial stress–strain curve has been chosen, the incremental plastic stress–strain relations can then be written as follows [1, 8]:

$$d\{\sigma\}^T = [C]_{ep}\, d\{\epsilon\}^T = ([C]_e - [C]_p)\, d\{\epsilon\}^T \quad (9)$$

$$[C]_e = \frac{E_c}{1-\nu^2}\begin{bmatrix} 1 & \nu & 0 \\ \nu & 1 & 0 \\ 0 & 0 & \frac{1-\nu}{2} \end{bmatrix} \quad (10)$$

$$[C]_p = \frac{[C]_e \frac{\partial g}{\partial\{\sigma\}^T}\frac{\partial f}{\partial\{\sigma\}}[C]_e}{\frac{E_c E_t}{(E_c - E_t)}\frac{G}{\sigma} + \frac{\partial f}{\partial\{\sigma\}}[C]_e\frac{\partial g}{\partial\{\sigma\}^T}}, \quad (11)$$

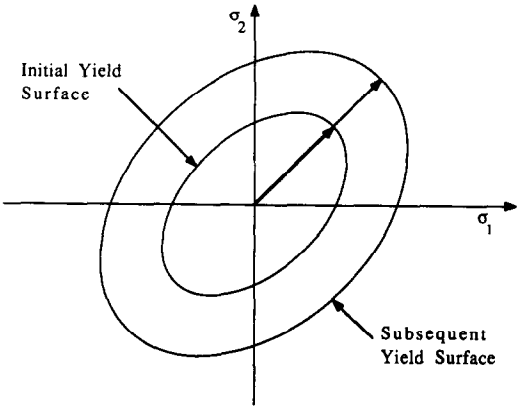

Fig. 4. Isotropic hardening rule.

where ν is Poisson's ratio for concrete and $g(\{\sigma\}, \sigma) = G(\{\sigma\}) - \sigma = 0$ is a plastic potential function. In this study, a nonassociated flow rule is used and the von Mises yield function is chosen as the plastic potential function. It has the following form:

$$g = \frac{3}{\sqrt{2}}\tau_{oct} - \sigma = 0. \quad (12)$$

There are several things worth noting in eqns (9) and (11). First, due to the use of the nonassociated flow rule (i.e. $g \neq f$), $[C]_{ep}$ is unsymmetrical, and in order to carry out a finite element solution an unsymmetrical equation solver is needed. Second, under the condition that $E_t = 0$, no matter how much the load is increased, the yield surface does not expand. Equation (9) then becomes the incremental stress–strain relationship for an elastic–perfectly plastic material and $[C]_{ep}$ is singular.

6. SINGLY CRACKED CONCRETE

In this study, a smeared crack model [9] is adopted. With this model the initiation of a cracking process at any location happens when the concrete stress reaches one of the failure surfaces either in the biaxial tension region or in a combined tension–compression region with $-\infty < \sigma_1/\sigma_2 < -1/15$. In the biaxial tension region, this surface has already been defined by eqn (4). In the combined tension–compression region the failure surface is defined by substituting f'_c for σ in eqn (5).

With the smeared crack representation, concrete is treated as an orthotropic material with principal axes normal and parallel to the crack direction (Fig. 6).

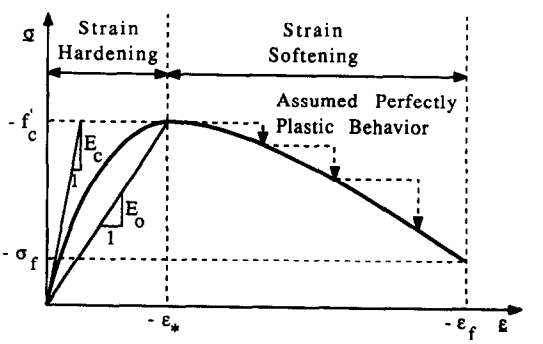

Fig. 5. Equivalent uniaxial stress–strain curve for concrete.

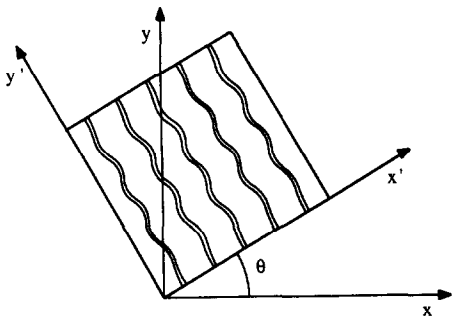

Fig. 6. Crack coordinates.

The incremental stress–strain relationships associated with the crack coordinates then become

$$[C'] = \begin{bmatrix} 0 & 0 & 0 \\ 0 & E_t & 0 \\ 0 & 0 & \mu G_c \end{bmatrix}, \tag{13}$$

where E_t is the tangent modulus of concrete parallel to the crack direction (choice of values discussed later), μ is the shear retention factor presented to provide for shear friction across the crack, and $G_c = E_c/2$ is the shear modulus for cracked concrete (the Poisson's ratio v is taken as zero due to the lack of interaction between the two orthogonal directions). Various forms of this shear factor have been proposed [10]. However, numerous analytical results have demonstrated that the particular value chosen for μ (between 0 and 1) does not appear to be critical, but values greater than zero are necessary to prevent numerical instabilities [10, 11]. Consequently, a constant value of $\mu = 0.25$ is used in this investigation.

7. TENSION STIFFENING

The use of an orthotropic constitutive relation, such as eqn (13), to describe cracked concrete does not represent the entire region that contributes to the definition of the stiffness. Intact concrete in the region also contributes. This, plus the fact that cracked concrete of a reinforced concrete element can still carry some tensile stress in the direction normal to the crack, constitutes a phenomenon termed tension stiffening. In this study, a general tension stiffening curve suggested by Bhide [12] is used. This curve is given as follows:

$$f_t = \frac{f'_t}{1 + 1000\epsilon_t(|\phi|/90)^{1.5}}, \tag{14}$$

where f_t and ϵ_t are the average tensile stress and the average tensile strain normal to the crack direction. ϕ is measured in degrees counterclockwise from the steel direction to the crack direction. In the case of unequal reinforcement in two orthogonal directions, the axis of the stronger reinforcement is taken as the reference direction. Equation (14) is plotted for various values of ϕ in Fig. 7.

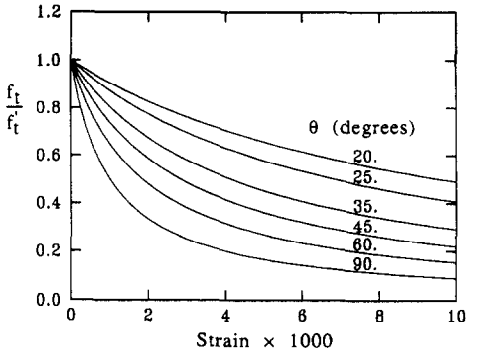

Fig. 7. Tension stiffening curves.

In situations where the reinforcing steel yields, the strain levels are sufficiently high that the average tensile stress of cracked concrete must be close to zero. Therefore, the tension stiffening effect should not artificially increase the total stress in the direction of any yielded reinforcement, otherwise an overestimation of the ultimate capacity may be expected. If there are L layers of steel existing at a concrete section, then a generalized upper bound for the concrete tension stiffening stress can be written as follows:

$$f_t \leqslant \sum_{i=1}^{L} \rho_i(f_{yi} - f_{si})\cos^2\theta_i, \tag{15}$$

in which f_{si} and f_{yi} are current stress (in tension) and yield stress, respectively, for the ith steel layer. θ_i is measured counterclockwise from the ith steel axis to the direction formal to the crack.

8. STRESS DEGRADING EFFECT FOR CONCRETE PARALLEL TO CRACK DIRECTION

After cracking has taken place, the concrete parallel to the crack direction is still capable of resisting either tensile or compressive forces. When it is subjected to tension, a pure linear elastic behavior is assumed (Fig. 8) and E_t is taken as E_c in eqn (13). On the other hand, when it is subjected to compression, experimental results [13] show that the tensile cracks have caused damage to the concrete with the transverse tensile strain having a degrading effect not only on the compressive strength but also on the

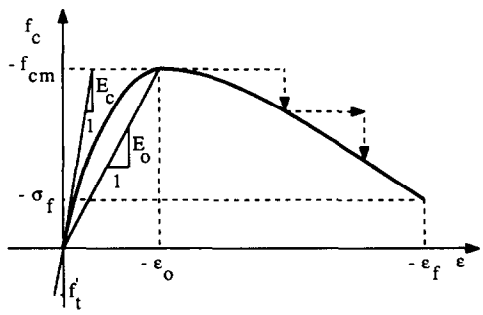

Fig. 8. Stress–strain curve for concrete parallel to the crack direction.

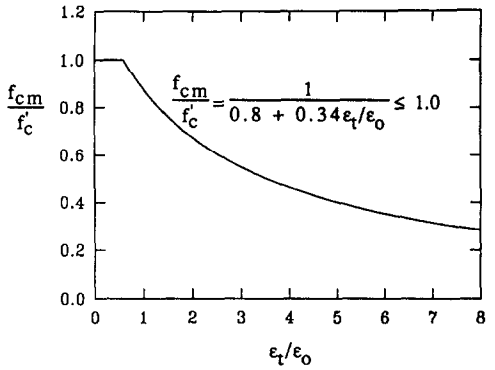

Fig. 9. Degraded maximum compressive strength for cracked concrete.

compressive stiffness. Therefore, concrete in this situation is softer and has weaker values than those recorded from a standard cylinder test. In this investigation, the experimentally determined relationship suggested by Vecchio and Collins [14] is used (Fig. 9). That relation is

$$\frac{f_{cm}}{f'_c} = \frac{1}{0.8 + 0.34\epsilon_t/\epsilon_o} \leqslant 1.0. \tag{16}$$

After the peak strength f_{cm} is determined, a stress–strain curve similar to eqn (7) is employed to calculate the concrete compressive stress f_c. We have (Fig. 8)

$$f_c = \frac{E_c\epsilon}{1 + (R + R_E - 2)\left(\frac{\epsilon}{\epsilon_o}\right) - (2R - 1)\left(\frac{\epsilon}{\epsilon_o}\right)^2 + R\left(\frac{\epsilon}{\epsilon_o}\right)^3}, \tag{17}$$

in which

$$R = \frac{R_E(R_\sigma - 1)}{(R_\epsilon - 1)^2} - \frac{1}{R_\epsilon} \qquad R_E = \frac{E_c}{E_o} \qquad R_\sigma = \frac{f_{cm}}{\sigma_f} \qquad R_\epsilon = \frac{\epsilon_f}{\epsilon_o} \qquad E_o = \frac{f_{cm}}{\epsilon_o}.$$

Again it is assumed that $R_\sigma = 4$ and $R_\epsilon = 4$. The tangent modulus, E_t, used in eqn (13) can then be calculated by differentiating eqn (17)

$$E_t = \frac{df_c}{d\epsilon} = \frac{E_c\left[1 + (2R - 1)\left(\frac{\epsilon}{\epsilon_o}\right)^2 - 2R\left(\frac{\epsilon}{\epsilon_o}\right)^3\right]}{\left[1 + (R + R_E - 2)\left(\frac{\epsilon}{\epsilon_o}\right) - (2R - 1)\left(\frac{\epsilon}{\epsilon_o}\right)^2 + R\left(\frac{\epsilon}{\epsilon_o}\right)^3\right]^2}. \tag{18}$$

It should be noted that due to this degrading of the maximum compressive strength, the tangent modulus is also reduced simultaneously. In order to prevent any numerical difficulty associated with negative tangent moduli, once the peak stress f_{cm} has been reached, E_t is set to zero and the unbalanced stresses are released in a stepwise fashion.

9. DOUBLY CRACKED CONCRETE

Upon further loading of single cracked concrete, a second set of cracks can form in the direction normal to the first set of smeared cracks. Therefore, in that direction, if the concrete stress is less than f'_t, then concrete remains singly cracked. Otherwise, if it is greater than f'_t, then the second set of cracks forms. The constitutive matrix for doubly cracked concrete is written as

$$[C'] = \begin{bmatrix} 0 & 0 & 0 \\ 0 & 0 & 0 \\ 0 & 0 & \mu G_c \end{bmatrix}, \tag{19}$$

while the tension stiffening stresses normal to both crack directions can be calculated by using eqn (14).

10. CONSTITUTIVE MATRIX FOR CRACKED CONCRETE

In most conventional finite element analysis of reinforced concrete structures, crack directions are assumed fixed once they form and while they remain open. This conception is termed the 'fixed crack model' [10]. However, this model leads to crack directions which may be inconsistent with the limit state [15]. The change in the crack direction and the consequential change in the direction of the maximum stiffness is clearly observed in the experimental work of Vecchio and Collins [13]. Therefore, a 'rotating crack model' [11, 15, 16] is employed in this study to include this behavior.

The basic assumption for the rotating crack approach is that after cracking takes place, the crack direction is always perpendicular to the direction of the major principal strain axis during the course of

loading. As a result, the rotating crack tangent constitutive matrix $[C]_c$ is the sum of the conventional tangent constitutive matrix for cracked concrete, plus a contribution which represents the effect of the possible changes in crack direction. This can be written as follows:

$$[C]_c = [T(\theta)]^T[C'][T(\theta)] + [G], \tag{20}$$

where $[G]$ matrix reflects the possible changes in the crack direction and

$$[T(\theta)] = \begin{bmatrix} \cos^2\theta & \sin^2\theta & \sin\theta\cos\theta \\ \sin^2\theta & \cos^2\theta & -\sin\theta\cos\theta \\ -2\sin\theta\cos\theta & 2\sin\theta\cos\theta & \cos^2\theta - \sin^2\theta \end{bmatrix} \tag{21}$$

is a transformation matrix in which θ is measured counterclockwise from global x-axis to crack x'-axis (Fig. 6).

This $[G]$ matrix in eqn (20) has been derived in detail in [11] and [15]. It has the following form:

$$[G] = \frac{(\sigma_x' - \sigma_y')\cos^2 2\theta}{2(\epsilon_x - \epsilon_y)} \begin{bmatrix} \sin^2 2\theta & -\sin^2 2\theta & -\sin 2\theta\cos 2\theta \\ -\sin^2 2\theta & \sin^2 2\theta & \sin 2\theta\cos 2\theta \\ -\sin 2\theta\cos 2\theta & \sin 2\theta\cos 2\theta & \cos^2 2\theta \end{bmatrix}. \tag{22}$$

For singly cracked concrete, $[C']$ in eqn (20) can be calculated by eqn (13). σ_x' and σ_y' in eqn (22) are the tension stiffening stress normal to the crack direction and the concrete stress parallel to the crack direction, respectively. For doubly cracked concrete, $[C']$ in eqn (20) can be calculated by eqn (19). σ_x' and σ_y' in eqn (22) are the tension stiffening stresses normal to the first crack and the second crack directions.

11. LAYERED MODEL

In the nonlinear finite element analysis of reinforced concrete structures, the element can be divided into a number of concrete layers through the thickness while the steel reinforcement is smeared into equivalent steel layers [11, 17] (Fig. 10). In this approach each concrete layer is assumed to be in a state of plane stress and the actual stress distribution of the concrete section is modeled by a piecewise constant approximation (Fig. 11). In addition, it is also assumed that the transverse shear stresses do not affect the inplane biaxial behavior of concrete. For each layer this approach is independent of the specific type of material properties present. Therefore, in the compression controlled region, the concrete layers might be in elastic, strain hardening and strain softening states while in the tension dominated area, the concrete layers could be in elastic, singly cracked and doubly cracked situations. The advantage of using this layered model is the generality of allowing for material property variation through the thickness of the section while not suffering the consequence of going to a complete three dimensional finite element analysis.

Let the concrete section be divided into K layers. The general stress–strain relatins for the jth layer are

$$\{\sigma\}^T = [C]_j\{\epsilon\}^T. \tag{23}$$

Assume $\{\epsilon_o\} = \{\epsilon_{xo}, \epsilon_{yo}, \gamma_{xyo}\}$ are the strains at the middle surface of the section and $\{\kappa\} = \{\kappa_x, \kappa_y, \kappa_{xy}\}$ are the curvatures. The strains at the mid-depth of the jth layer can be calculated as follows:

$$\{\epsilon\}^T = \{\epsilon_o\}^T + z_j\{\kappa\}^T, \tag{24}$$

where z_j is the distance between the center of the jth layer and the middle surface of the section. Let z_{jt} and

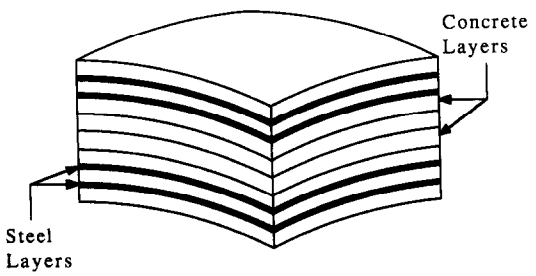

Fig. 10. Layered model.

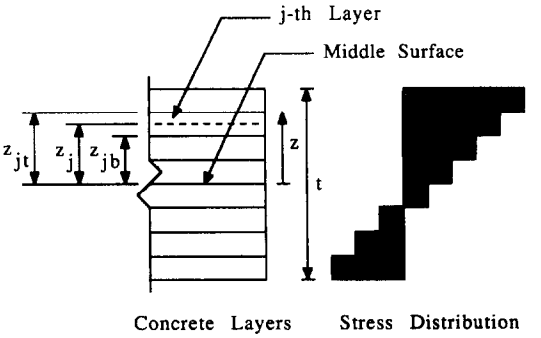

Fig. 11. Stress profile for concrete section.

z_{jb} be the distance from the middle surface of the section to the top and bottom of the jth layer, respectively. Then, the stress resultants for the jth layer are

$$\{N\}^T = (z_{jt} - z_{jb})\{\sigma\}^T \quad \{M\}^T = z_j(z_{jt} - z_{jb})\{\sigma\}^T, \tag{25}$$

where $\{N\} = \{N_x, N_y, N_{xy}\}$, $\{M\} = \{M_x, M_y, M_{xy}\}$. Substituting eqns (23) and (24) into eqn (25), the contribution of the jth layer to the various stress resultants can be expressed in the following form:

$$\begin{Bmatrix}\{N\}^T \\ \{M\}^T\end{Bmatrix}_j = \begin{bmatrix}(z_{jt} - z_{jb})[C]_j & z_j(z_{jt} - z_{jb})[C]_j \\ z_j(z_{jt} - z_{jb})[C]_j & z_j^2(z_{jt} - z_{jb})[C]_j\end{bmatrix}\begin{Bmatrix}\{\epsilon_o\}^T \\ \{\kappa\}^T\end{Bmatrix}. \tag{26}$$

Summing the stiffness contributions of each layer together, the stiffness matrix for the concrete section can be expressed as

$$\begin{Bmatrix}\{N\}^T \\ \{M\}^T\end{Bmatrix} = \sum_{j=1}^{K}\begin{bmatrix}(z_{jt} - z_{jb})[C]_j & z_j(z_{jt} - z_{jb})[C]_j \\ z_j(z_{jt} - z_{jb})[C]_j & z_j^2(z_{jt} - z_{jb})[C]_j\end{bmatrix}\begin{Bmatrix}\{\epsilon_o\}^T \\ \{\kappa\}^T\end{Bmatrix}. \tag{27}$$

The $[C]_j$ matrix used in eqn (27) may be $[C]_e$ of eqn (10) if the jth concrete layer is elastic, or may be $[C]_{ep}$ of eqn (9) if the jth concrete layer is plastic, or may be $[C]_c$ of eqn (20) if the jth concrete layer is cracked.

In the layered approach, the steel reinforcement is smeared into equivalent layers of steel having uniaxial properties and the stress distribution of reinforcement is considered to be discrete in the section (Fig. 12). Similar to concrete, the stiffness matrix for reinforcing steel (assumed L layers in total) can be written as

$$\begin{Bmatrix}\{N\}^T \\ \{M\}^T\end{Bmatrix} = \sum_{i=1}^{L}\begin{bmatrix}2[C]_i & 2z_i[C]_i \\ 2z_i[C]_i & 2z_i^2[C]_i\end{bmatrix}\begin{Bmatrix}\{\epsilon_o\}^T \\ \{\kappa\}^T\end{Bmatrix} \tag{28}$$

$$[C]_i = [T(\phi_i)^T][C]_{si}[T(\phi_i)], \tag{29}$$

where z_i is the distance between the mid-depth of the ith steel layer and the middle surface of the section. ϕ_i is the direction angle of the ith reinforcement (Fig. 1). the $[C]_{si}$ matrix used in eqn (29) may be either that of eqn (1) or that of eqn (2), depending on whether the state of the ith steel layer is elastic or plastic.

In the layered stiffness formulation, the steel reinforcement is assumed to be unaffected by any transverse shear stresses. The transverse shear stresses are all applied to the concrete section and would not affect the inplane and the flexural behavior of the concrete layers. Furthermore, these transverse shear stresses are assumed to always remain elastic and are not included in the yielding or cracking processes. The matrix relation between transverse shear stresses and transverse shear strains becomes

$$\begin{Bmatrix}\tau_{xz} \\ \tau_{yz}\end{Bmatrix} = [C]\begin{Bmatrix}\gamma_{xz} \\ \gamma_{yz}\end{Bmatrix} \quad [C] = \begin{bmatrix}\dfrac{G}{\alpha'} & 0 \\ 0 & \dfrac{G}{\alpha'}\end{bmatrix}, \tag{30}$$

where G is the shear modulus of concrete and α' is a correction factor for shear to account for the shape of the cross section and is usually taken as 1.2.

The shear forces can be obtained by integrating the shear stresses through the thickness and the relationship between the transverse shear forces $\{Q\} = \{Q_x, Q_y\}$ and the transverse shear strains $\{\gamma_t\} = \{\gamma_{xz}, \gamma_{yz}\}$ can be expressed as follows:

$$\{Q\}^T = t[C]\{\gamma_t\}^T. \tag{31}$$

For the reinforced concrete section, the final form of the stress resultant constitutive matrix at an integration point can be written as

$$\begin{Bmatrix}\{N\}^T \\ \{Q\}^T \\ \{M\}^T\end{Bmatrix} = [D]\begin{Bmatrix}\{\epsilon_o\}^T \\ \{\gamma_t\}^T \\ \{\kappa\}^T\end{Bmatrix}, \tag{32}$$

where $[D]$ can be established by assembling the contributions of all the concrete layers via eqn (27), those of all the steel layers via eqn (28), and that for the transverse shear stiffness via eqn (31).

It should be noted that in the reinforced concrete section, there are different stress states existing in the different layers. Some concrete layers may crack in tension while others may yield in compression. Steel layers may yield in tension or compression. Generally, the stress resultant constitutive matrix is no longer symmetric with respect to the middle surface and the extensional and flexural terms are coupled.

For the finite element analysis, one of the important decisions to be made is to determine the adopted

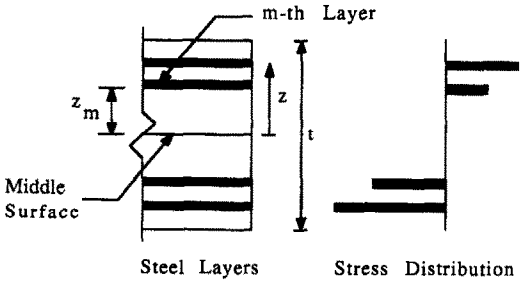

Fig. 12. Stress profile for steel reinforcement.

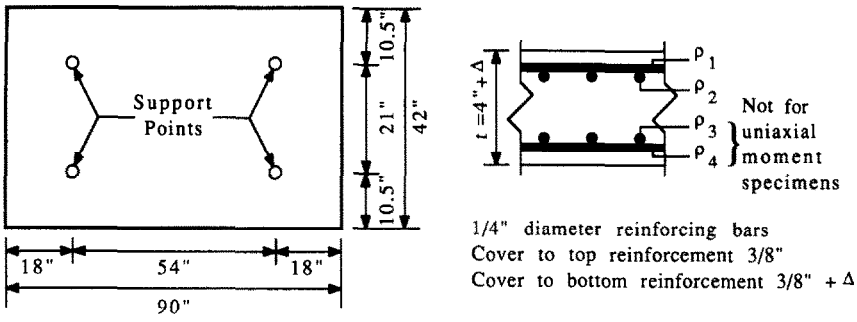

Dimensions of test specimens Cross section

Fig. 13. Cardenas–Sozen specimens.

number of concrete layers which represents the cross section of the structures. In [11] and [18], it has been shown that the results and costs of analyses are not sensitive to the number of concrete layers. Therefore, a total of 10 concrete layers is used in the following examples.

12. NUMERICAL EXAMPLES

12.1. *Slabs in uniform flexural force fields*

To evaluate the ability of the proposed definitions of material response in modeling the flexural behavior of reinforced concrete structures, the best starting point is to test them against structures that are subjected to uniform flexural forces. For this purpose, the experimental work of Cardenas and Sozen [19] is chosen.

The dimensions of the reinforced concrete slabs and the details of the slabs' cross section are shown in Fig. 13. In this set of examples, nine specimens with varying orientations of reinforcement and varying steel percentages are studied. Among them slabs B7, B11 and B12 are subjected to uniaxial moment, slabs B15, B16 and B17 are subjected to pure torsion, while

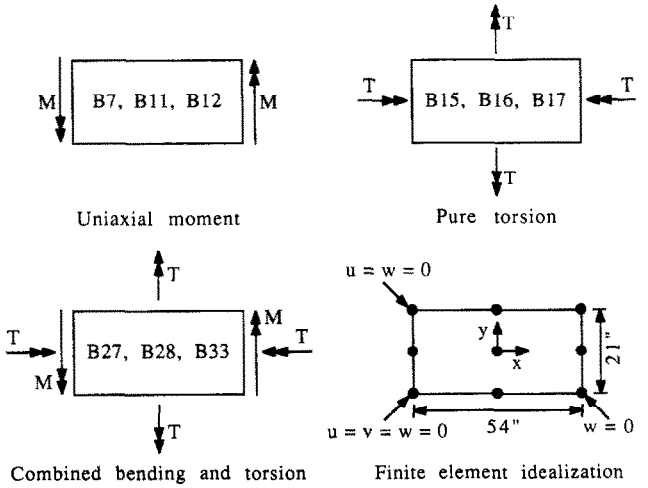

Uniaxial moment Pure torsion

Combined bending and torsion Finite element idealization

Fig. 14. Loading pattern and finite element idealization for Cardenas–Sozen specimens.

Table 1. Material properties for Carden-Sozen specimens

Slab	Thickness t (in.)	Thickness Δ (in.)	Concrete f'_c (psi)	f_y (ksi)	Reinforcement ρ_1 and ρ_4	Reinforcement ρ_2 and ρ_3	Reinforcement ϕ_1 and ϕ_4 (deg.)†	Reinforcement ϕ_2 and ϕ_3 (deg.)†	Loads Ratio of T/M
B7	4.14	0.14	5150	50.0	0.00790	0.00862	135.0	45.0	0
B11	4.12	0.12	4800	50.0	0.00794	0.00433	157.5	67.5	0
B12	4.12	0.12	5170	47.6	0.00794	0.00433	67.5	157.5	0
B15	4.09	0.09	5260	47.9	0.00800	0.00873	135.0	45.0	∞
B16	4.04	0.04	4730	48.3	0.00810	0.00884	90.0	0.0	∞
B17	4.03	0.03	5530	50.8	0.00812	0.00886	157.5	67.5	∞
B27	4.06	0.06	5350	45.2	0.00806	0.00879	135.0	45.0	0.45
B28	4.08	0.08	5620	47.6	0.00802	0.00875	157.5	67.5	0.45
B33	4.07	0.07	4930	45.9	0.00804	0.00219	0.0	90.0	0.45

†Measured counterclockwise from x-axis.

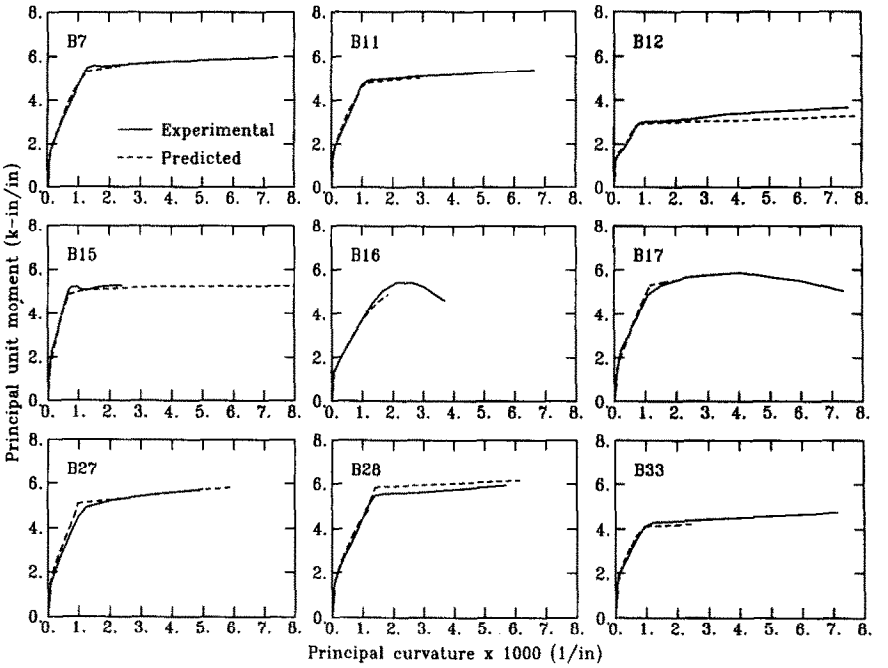

Fig. 15. Moment–curvature plot for Cardenas–Sozen specimens.

Table 2. Experimental and numerical results for Cardenas–Sozen specimens

	Experimental			Predicted		
Slab	M_y (k-in./in.)	M_u (k-in./in.)	θ_u (deg.)	M_y (k-in./in.)	M_u (k-in./in.)	θ_c (deg.)
B7	5.60	5.85	90	5.32	5.79	90
B11	4.50	5.35	109	4.59	5.01	107
B12	2.80	3.82	80	2.94	3.27	84
B15	5.20	5.33	135	4.87	5.39	135
B16	5.43	5.43	135	4.93	4.93	135
B17	5.50	5.88	135	5.31	5.54	127
B27	5.00	5.70	111	5.10	5.84	109
B28	5.40	5.90	113	5.86	6.17	110
B33	4.18	4.60	137	4.12	4.22	135

M_y: yield moment.
M_u: ultimate moment.
θ_u: yield line orientation.
θ_c: orientation of the normal to principal strain direction in top cracked concrete layer.
(Positive angles are measured counterclockwise from x-axis.)

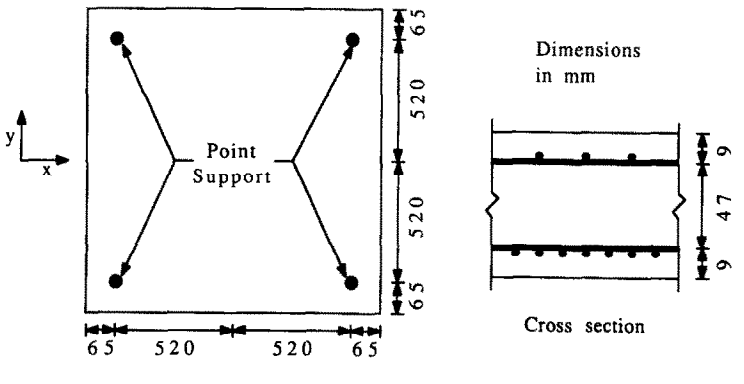

Fig. 16. Duddeck–Griebenow–Schaper specimens.

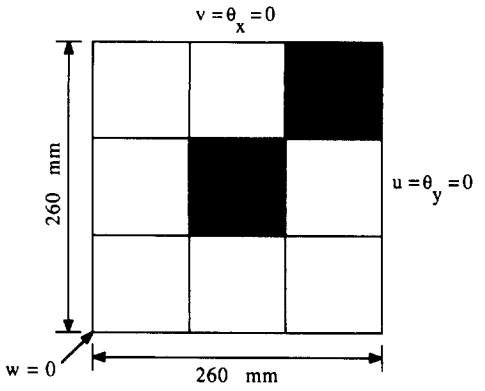

Fig. 17. Finite element idealization for Duddeck–Griebenow–Schaper specimens.

slabs B27, B28 and B33 are subjected to combined bending and torsion. The loading patterns for these three groups of specimens are shown in Fig. 14. In the finite element analysis, a single nine-node Lagrangian shell element with reduced integration (2 × 2) rule is used to model these reinforced concrete slabs (Fig. 14). The details of concrete properties and steel information are listed in Table 1. In addition, it is assumed that $\epsilon_o = 0.003$, $v = 0.19$, $f_t' = 4\sqrt{f_c'}$ psi, $E_c = 57{,}000\sqrt{f_c'}$ psi, $E_s = 30 \times 10^6$ psi and $E_{sp} = 0.01E_s$ for all the slabs.

The comparisons of the predicted and the experimental results of these test slabs are plotted in moment–curvature diagrams as shown in Fig. 15 and are summarized in Table 2. It is seen from the figure that the proposed reinforced concrete material model is satisfactory in modeling the behavior of these specimens, not only in the elastic stage but also in the plastic and the cracking stages. Generally, the calculated yield moments and the ultimate moment as well as the predicted yield line orientation are in good agreement with the experimental results.

12.2. *Corner supported slabs*

In this example, two corner supported slabs, S11 and S31, tested by Duddeck *et al.* [20], are studied. Though slab S11 is isotropically reinforced and slab S31 is anisotropically reinforced in the x and y directions, the total amount of steel reinforcement is equal for these two specimens. Both slabs are subjected to a concentrated loading applied at the center of the slab and both of them have well defined boundary conditions in which only the transverse deflections at the corner supports are restrained.

Because of the meager information given in [20], details of these slabs have been taken from [16] and [18]. The dimensions and cross section of the specimens are shown in Fig. 16 while the input material properties are given in Table 3.

In this example, due to the symmetry of the structure and the loading, only a quarter of the slab is analyzed. The finite element idealization as well as the boundary conditions are shown in Fig. 17, where nine nine-node Lagrangian shell elements are used. In order to suppress the spurious zero energy modes, a full integration (3 × 3) rule is applied to two select elements, while the rest of the elements are still integrated by the reduced integration (2 × 2) rule. The positions of these fully integrated elements are shown as shaded areas in the finite element meshes (Fig. 17).

The calculated load–central deflection curves for specimens S11 and S31 are compared with the test results in Fig. 18. Crack patterns for these two slabs and the status of yield conditions in the reinforcement at the numerical integration points for the last load step are given in Figs 19 and 20.

Generally, the results predicted by the numerical simulation are in good agreement with the limited experimental deflection data. The predicted limit loads (64.0 kN for slab S11 and 34.5 kN for slab S31)

Table 3. Material properties for Duddeck–Griebenow–Schaper specimens

Slab	f_c' (MPa)	f_t' (MPa)	E_c (MPa)	v	f_y (MPa)	Top ρ_x (%)	Top ρ_y (%)	Bottom ρ_x (%)	Bottom ρ_y (%)
S11	43	2	16400	0.19	670	0.297	0.297	0.611	0.611
S31	43	2	16400	0.19	670	0.435	0.158	0.895	0.326

$\epsilon_o = 0.0027$; $E_s = 201000$ MPa; $E_{sp} = 2010$ MPa.

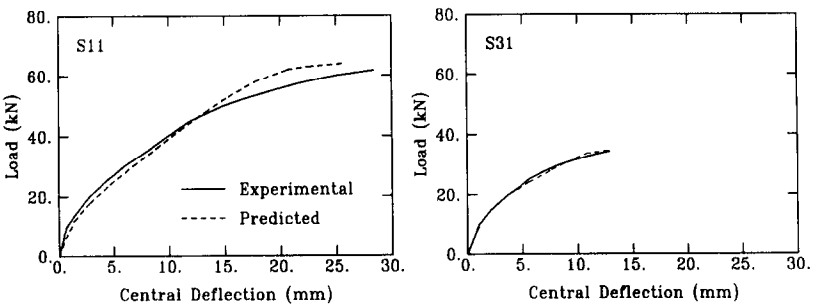

Fig. 18. Load–deflection plot for Duddeck–Griebenow–Schaper specimens.

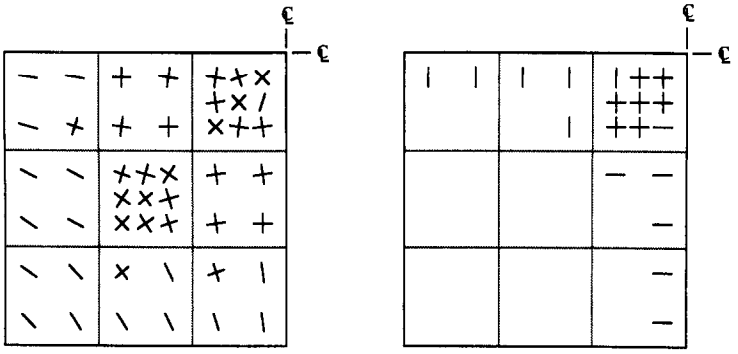

Crack pattern for bottom concrete layer Yielded reinforcement in bottom layer

Fig. 19. Crack pattern and yielded reinforcement for slab S11.

are very close to the experimental results (61.7 kN for slab S11 and 34.3 kN for slab S31). In addition, the numerical solution predicts the failure mechanism, which is the bottom steel yielding near the load point, for both slabs correctly.

12.3. *Diaphragm supported cylindrical shell*

The final example is a cylindrical shell with edge beams which has been tested by Harris and White [21]. This shell, LC1, is a model constructed of reinforced mortar. It has rigid end diaphragms which are simply supported at the four corners. This shell is subjected to gravity load applied to 72 points on the shell surface through an articulated system which reduces to a single force applied with a jack. The shell surface is therefore drilled with 72 holes to allow the tension load cell rods (diameter = 0.5 in.) to pass through. In this investigation, these holes are not considered; the entire shell surface is asasumed to remain solid.

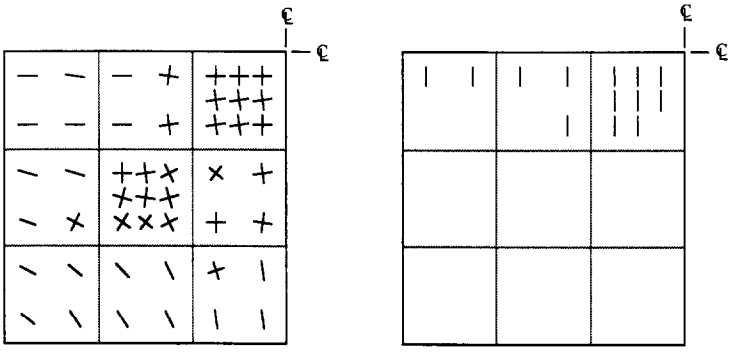

Crack pattern for bottom concrete layer Yielded reinforcement in bottom layer

Fig. 20. Crack pattern and yielded reinforcement for slab S31.

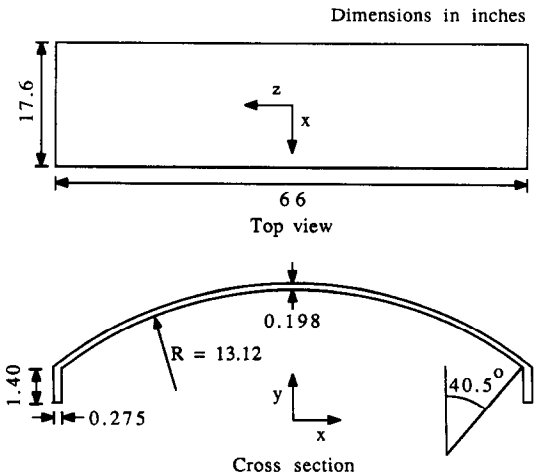

Fig. 21. Harris–White specimen.

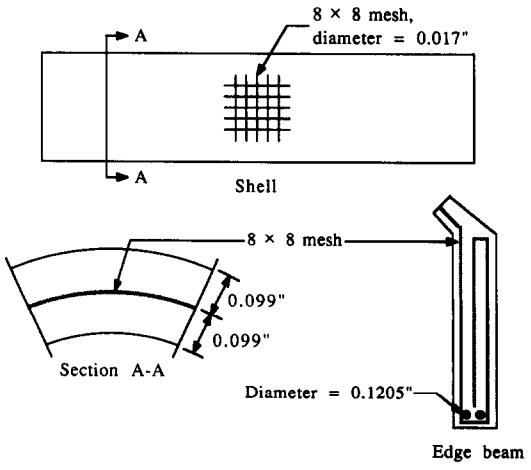

Fig. 22. Reinforcing details for Harris–White specimen.

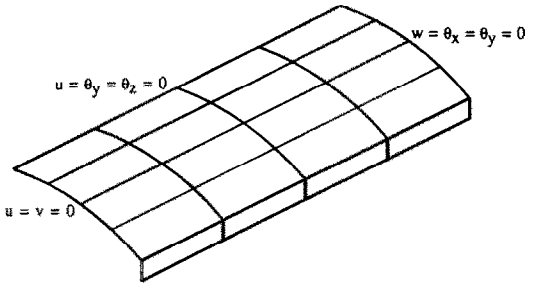

Fig. 23. Finite element idealization for Harris–White specimen.

Dimensions of shell LC1 are given in Fig. 21 while the reinforcing details are shown in Fig. 22. A commercial woven steel mesh with 0.017-in. diameter wires at 0.125 in. spacing in both directions was used for the shell. This mesh was further carried into the edge beam and acted as the tensile and shear reinforcement. Additional tensile reinforcing steel was provided in the beams by adding two 0.1205-in. diameter wires at the bottom of each edge beam. The material properties used are given as follows: $\epsilon_o = 0.003$, $\nu = 0.19$, $f'_c = 4600$ psi, $f'_t = 607$ psi, $E_c = 3.45 \times 10^6$ psi, $f_y = 42{,}000$ psi, $E_s = 29.8 \times 10^6$ psi, and $E_{sp} = 0$. It must be acknowledged that this is a mortar model not a reinforced concrete shell. Some differences in material behavior exist but verification is on a method using mortar properties.

Due to the symmetry of the structure and the loading, only a quarter of the shell is analyzed. The finite element idealization and the boundary conditions are shown in Fig. 23, where 20 nine-node Lagrangian shell elements are used. in order to model the additional tensile reinforcing steel in the edge beams, an extra eight truss elements with elastic–perfectly plastic material properties are used and placed at the bottom of the edge beam. In the numerical analysis, every nonlinear nine-node element is overlaid with an elastic eight-node element whose modulus of elasticity is of 10^{-3} times that used for the nonlinear element [16]. All the linear and nonlinear shell elements are integrated by the reduced integration (2×2) rule. It is found that this overlaid technique is sufficient to suppress the zero energy modes and satisfactory results are obtained.

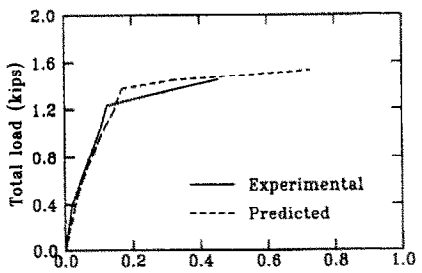

Fig. 24. Load–deflection plot for shell LC1.

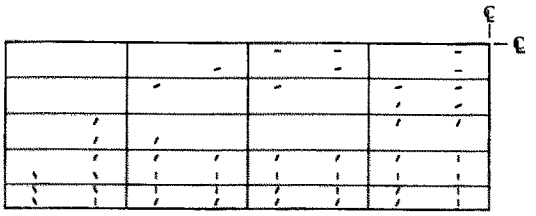

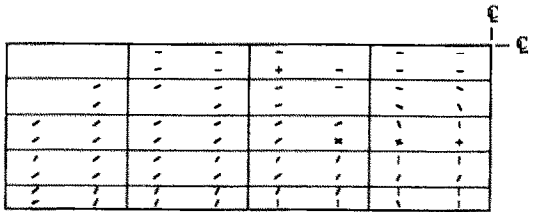

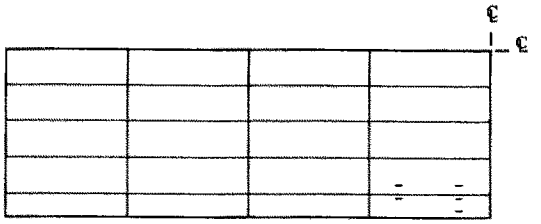

Fig. 25. Crack pattern and yielded reinforcement for shell LC1.

The deflections at the midspan of edge beams are plotted against the total load applied to the shell surface in Fig. 24. The predicted crack pattern for the shell and the status of yield conditions in the reinforcement at the integration points for the last load step are shown in Fig. 25.

In general, the correlation is good between the analytical and experimental curves. The predicted failure load, 1.55 k, is in good agreement with the experimental ultimate load, 1.45 k. Furthermore, the predicted failure mechanism which is the yielding of the reinforcement in the shell as well as in the edge beams is also very consistent with the experimental result.

13. CONCLUSION

As a conclusion, the good agreement obtained in these sets of examples between the numerical predictions and the experimental results establishes the validity and accuracy of using the proposed reinforced concrete material model in modeling the flexural behavior as well as the combined membrane–flexural behavior of reinforced concrete plate and shell structures.

Acknowledgements—This work was financially supported by the National Science Foundation under grant number NSF CEE 83-00226.

REFERENCES

1. H.-T. Hu and W. C. Schnobrich, Constitutive modelling of concrete by using nonassociated plasticity. *J. Mater. Civ. Engng, ASCE* **1**(4), 199–216 (1989).
2. H.-T. Hu and W. C. Schnobrich, Nonlinear analysis of cracked reinforced concrete. *ACI struct. Jnl* **87**, 199–207 (1990).
3. H. Kupfer, H. K. Hilsdorf and H. Rusch, Behavior of concrete under biaxial stresses, *ACI Jnl, Proc.* **66**, 656–666 (1969).
4. L. P. Saenz, Discussion of "Equation for the stress–strain curve of concrete," by Desayi, P. and Krishnan, S. *ACI Jnl, Proc.* **61**, 1229–1235 (1964).
5. D. Darwin and D. A. Pecknold, Inelastic model for cyclic biaxial loading for reinforced concrete. Civil Engng Studies, SRS 409, University of Illinois, Urbana, IL (1974).
6. A. A. Elwi and D. W. Murray, A 3D hypeoelastic concrete constitutive relationship. *J. Engng Mech. Div., ASCE* **105**(EM4), 623–641 (1979).
7. E. Y.-T. Chen, Numerical simulation of reinforced concrete subjected to multiaxial stress conditions. Ph.D. thesis, University of Illinois, Urbana, IL (1981).
8. W. F. Chen, *Plasticity in Reinforced Concrete*. McGraw–Hill, New York (1982).
9. Y. R. Rashid, Ultimate strength analysis of prestressed concrete pressure vessels. *Nucl. Engng Des.* **7**, 334–344 (1968).
10. ASCE Task Committee on Concrete and Masonry Structure, State of the Art Report on Finite Element Analysis of Reinforced Concrete. ASCE, New York (1982).
11. H.-T. Hu and W. C. Schnobrich, Nonlinear analysis of plane stress state reinforced concrete under short term monotonic loading. Civil Engng Studies, SRS 539, University of Illinois, Urbana, IL (1988).
12. S. B. Bhide, Reinforced concrete elements in shear and tension. Ph.D. thesis, University of Toronto, Ontario (1986).
13. F. Vecchio and M. P. Collins, The response of reinforced concrete to in-plane shear and normal stresses. Publication No. 82-03, University of Toronto, Ontario (1982).
14. F. J. Vecchio and M. P. Collins, The modified compression-field theory for reinforced concrete elements subjected to shear. *ACI Jnl, Proc.* **83**, 219–231 (1986).
15. A. K. Gupta and H. Akbar, Cracking in reinforced concrete analysis. Reinforced Concrete Shell Research Report, Civil Engineering Department, North Carolina State University, Raleigh, NC (1983).
16. R. V. Milford and W. C. Schnobrich, Nonlinear behavior of reinforced concrete cooling towers. Civil Engng Studies, SRS 514, University of Illinois, Urbana, IL (1984).
17. F. R. Hand, D. A. Pecknold and W. C. Schnobrich, A layered finite element nonlinear analysis of reinforced concrete plates and shells. Civil Engng Studies, SRS 389, University of Illinois, Urbana, IL (1972).
18. H. H. Abdel Rahman, Computational models for the nonlinear analysis of reinforced concrete flexural slab system. Ph.D. thesis, University College of Swansea, Swansea (1982).
19. A. Cardenas and M. A. Sozen, Strength and behavior of isotropically and nonisotropically reinforced concrete slabs subjected to combinations of flexural and torsional moments. Civil Engng Studies, SRS 336, University of Illinois, Urbana, IL (1968).
20. H. Duddeck, G. Griebenow and G. Schaper, Material and time dependent nonlinear behaviour of cracked reinforced concrete slabs. In *Nonlinear Behaviour of Reinforced Concrete Spatial Structures, Vol.* I, *Preliminary Report*, IASS Symposium, Darmstadt (Edited by G. Mehlhorn, H. Ruhle and W. Zerna), pp. 101–103. Werner, Dusseldorf (1978).
21. H. G. Harris and R. N. White, The inelastic analysis of concrete cylindrical shells and its verification using small scale models. Report No. 330, Department of Structural Engineering, School of Civil Engineering, Cornell University, Ithaca, NY (1967).